RSC Advances

ROYAL SOCIETY
OF CHEMISTRY

www.rsc.org/advances

A table of contents entry
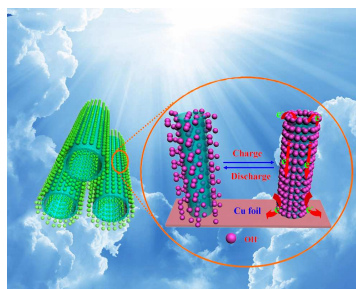
Porous CuO nanotube electrode synthesized by *in situ* oxidation of copper foils exhibits superior pseudocapacitive and electrocatalytic performances.

ARTICLE TYPE

Cost-Effective CuO Nanotube Electrodes for Energy Storage and Non-enzymatic Glucose Detection

Yang Lu,[a,b,c] Kangwen Qiu,[a,b] Deyang Zhang,[a,b,d] Jing Lin,[c] Jinyou Xu,[a, b] Xianming Liu,[e] Chengchun Tang,*[c] Jang-Kyo Kim,[f] Yongsong Luo,*[a,b]

A facile strategy is developed to *in situ* synthesize low-cost, freestanding, binder-free CuO nanotube electrodes on a conducting Cu foil, totally eliminating non-active materials and extra processing steps. The synergy arising from the ameliorating structure, such as high porosity, large surface area and the
10 ability for fast electron transport, the CuO nanotube electrodes can make an ideal multi-functional electrochemical device with excellent pseudocapacitive performance and a remarkable sensitivity to glucose as non-enzymatic biosensor (NGB). The electrodes deliver remarkable specific capacitances of 442 and 358 F g^{-1} at current densities of 1 and 20 A g^{-1}, respectively. The capacitance loss after 5000 cycles is only 4.6% at 1 A g^{-1}, a reflection of excellent cyclic stability of the supercapacitor. The biosensor made from CuO
15 nanotubes present an extremely rapid and accurate response to glucose in blood in a wide, linear range of 100 µM to 3 mM with a sensitivity of 2231 µA mM^{-1} cm^{-2}. These interesting discoveries may open potentials for further developing new, multi-functional electrodes possessing both excellent energy storage and biosensory capabilities.

Introduction

20 Efficient energy storage and its economic use are central to the development of modern electronic products, transportation systems and medical devices.[1] Supercapacitors (SCs) can offer higher power densities with longer cyclic lifespans than rechargeable batteries, and store higher energy densities than
25 conventional capacitors,[2-6] thus have been considered one of the most promising next-generation energy storage devices. A major bottleneck that hinders practical applications of existing SCs to date, however, is the lack of low-cost, high performance electrode materials. Porous nanostructures deposited directly on conductive
30 metal substrates have been developed as electrodes possessing large active surface areas, capability to buffer the volume change during the charge/discharge process and short pathway for electron/ion transport.[7-14] Among various porous materials, mesoporous CuO has attracted considerable interest for SC
35 application due to its low cost, excellent pseudocapacitive behavior, environmental benignity and practical availability.[15-17]

On the other hand, biosensors are important for clinical diagnostics, biological and chemical analyses and environmental monitoring.[18-20] Diabetes is a well-known global health care
40 problem that seriously affects daily life of hundreds of millions of people.[21] To dynamically monitor the concentration of glucose in the blood is an essential component of modern diabetes management, including clinical detection and therapy.[22] In the past, the vast majority of glucose monitoring was carried out
45 using enzymatic sensors because of their high selectivity, excellent sensitivity and low detection limit. However, enzymatic

sensors suffer from not only the instability, but also the complexity and poor reproducibility.[23] To address the above issues, significant research has been directed towards developing
50 non-enzymatic sensors based on noble metals, such as Pt and Au, alloys and metal oxides.[24-27] Compared with noble metals and alloys, CuO-based electrodes exhibited a higher electrocatalytic oxidation ability for glucose. Especially, nanostructured CuO possesses a large specific surface area, excellent electrochemical
55 activity and high electron transfer reactions at a low overpotential,[28, 29] making it a promising candidate for non-enzymatic sensor applications. For instance, CuO nanowires demonstrated a high stability and good selectivity in glucose determination.[30] CuO/graphene nanocomposites have also shown
60 a good electrocatalytic activity for oxidation of glucose in an alkaline medium at room temperature.[31]

As an important transition metal oxide, CuO has been synthesized using various methods such as hydrothermal method, electrodeposition, chemical bath deposition and electrostatic spinning.
65 In order to prepare electrode of supercapacitor and biosensor using CuO powders as the active material, the CuO powder is generally mixed with binders and conducting additives to obtain a paste. Such obtained electrodes often suffer drawbacks of low active material utilization due to the presence of inaccessible regions to the
70 electrolyte. It has been demonstrated that electrodes of one-dimension arrays standing on a conductive substrate usually holds larger electrochemical active surface area and higher utilization efficiency of the active materials than conventional powder electrodes. For example, Yang et al. reported a solution-immersion
75 strategy for growing Cu(OH)$_2$/CuO nanotube arrays, which show

good non-enzymatic electrocatalytic responses to glucose in alkaline media.[32]

Herein, we develop a facile, low-cost method for the synthesis of porous CuO nanotubes through *in situ* oxidation of commercial copper foils, followed by low-temperature annealing. The whole process can be scaled up for mass production. The freestanding CuO nanotube electrodes are multi-functional: they can serve as high-performance SC, as well as high sensitivity non-enzymatic glucose biosensor (NGB). The electrodes developed in this study have several unique material and structural features that other types of electrodes are lacking. (I) Cu foils offer many advantages due to natural abundance, excellent electrical conductivity, low cost and flexibility. (II) CuO nanotubes grown directly on the surface of current collector can be directly used as freestanding electrode while totally eliminating binders and conducting additives as well as extra steps to assemble them. The fully integrated CuO nanotube/Cu foil structure means extremely low contact resistance with fast electron/ion transport and high rate capability. (III) The intrinsically large surface area of the nanotube forest offers numerous active sites and full utilization of electrode materials with high specific capacitance and excellent sensitivity to glucose detection. (IV)There are plenty of void space and pores between the neighbouring nanotubes allowing full penetration of the electrolyte or glucose solution.

Experimental

Growth of CuO nanotubes on Cu Foil

All the reagents were of analytical grade and used without further purification. In a typical process, 10 mm x 10 mm square Cu foils of 0.5 mm in thickness and 99.9% purity (Alfa Aesar) were washed in a 3 M HCl aqueous solution for 15 min to remove the surface impurities and oxide layers. Immediately after rinsing several times with ethanol and distilled water, the Cu foils were immersed in the aqueous solution containing 2.5 M NaOH and 0.125 M $(NH_4)_2S_2O_8$ at room temperature for the growth of $Cu(OH)_2$ nanotubes. The gold colour of the Cu foil gradually changed to faint blue while the initially colourless solution also became blue. After 20 min of treatment, the Cu foils with a layer of $Cu(OH)_2$ nanotubes were taken out of the solution, rinsed with deionized water and ethanol, and dried in air. To obtain CuO nanotubes, the $Cu(OH)_2$ nanotubes on a Cu foil were annealed at 150 ^{o}C for 1 h to complete dehydration, and then the temperature was elevated to 200 ^{o}C and kept for another 2 h to promote crystallization in a nitrogen atmosphere. Finally, the CuO nanotube/Cu foil composites were naturally cooled to ambient.

Characterization

Thermogravimetric and differential thermal analysis (TG-DTA, SDT 2960) was conducted at a heating rate of 10 ^{o}C min^{-1} in a nitrogen atmosphere. The phase structure of the materials were characterized by X-ray diffraction (XRD) on a D8 Focus (Bruker, Germany) automated X-ray diffractometer system with Cu-Kα radiation (λ=1.5418 Å). The Raman scattering measurement was carried out on a laser Raman spectrometer (Renishaw, England) at room temperature. The morphologies and microstructures were characterized by field emission scanning electron microscopy (FSEM, JEOL S-4800) and transmission electron microscopy (TEM, JEOL JEM-2010). Specific surface areas were measured

on a Quadrasorb SI-MP Surface Area and Porosity Analyzer (American, Quantachrome) at 77 K using the Brunauer-Emmett-Teller (BET) method with nitrogen adsorption. The pore size distributions were obtained by means of the Barrett-Joyner-Halenda (BJH) equation using the adsorption isotherm branch. The static contact angles (CAs) were measured according to the sessile-drop method using a contact angle analyzer (Kino SL200B, American) with water at ambient temperature. The size of the water droplet was ~ 5 μL. The average CA value was obtained by measuring several different positions for the same sample.

Electrochemical analyses

CuO nanotubes on a Cu foil were directly used as electrode without adding conductive agent or binder. The average mass loading of CuO on a Cu foil was ~2.5 mg cm^{-2}. The pseudocapacitive performance of the CuO nanotube/Cu foil electrodes was investigated on an electrochemical workstation, CHI660E (Chenhua, P. R. China) using a three-electrode system. The composite electrode was used as the working electrode while a Pt foil and Hg/HgO served as the counter electrode and the reference electrode, respectively, with a solution of 1 M KOH as the electrolyte at room temperature. Cyclic voltammetry (CV) analysis was performed between -0.5 and 0.1 V *vs.* Hg/HgO at scan rates from 5 to 100 mV s^{-1}. Galvanostatic charge/discharge tests were conducted in a stable potential window at different current densities of 1-20 A g^{-1}. Electrochemical impedance spectroscopy (EIS) was performed at an AC voltage of 5 mV in the frequency range from 0.01 Hz to 100 kHz.

The electrocatalytic activities of the CuO nanotube/Cu foil electrodes for oxidation of glucose were investigated in 0.1 M KOH electrolyte solution on a CHI660E electrochemical workstation in ambient condition. A standard three-electrode system was employed which consisted of a CuO nanotube working electrode, a Pt foil counter electrode and an Ag/AgCl reference electrode. Linear-sweep voltammetry measurements were carried out in the potential range of 0-0.8 V *vs.* Ag/AgCl. A proper amount of glucose was successively added into the 0.1 M KOH solution while continuously stirring to perform the amperometric study.

Results and discussion

Structures and morphologies

Fig. 1a schematically illustrates the synthesis process of CuO nanotubes. The growth of $Cu(OH)_2$ and CuO nanotubes can be visually tracked by the color changes of the Cu foil. The fresh Cu foil exhibited a gold color with a glossy surface (Fig. 1b). During the treatment in the alkaline solution, the surface color gradually changed to light blue and lost its luster (Fig. 1c), consistent with *in situ* growth of $Cu(OH)_2$ nanotubes directly on the Cu foil substrate. The $Cu(OH)_2$ nanotubes were finally transformed to black CuO nanotubes after annealing (Fig. 1d). The corresponding SEM images reveal that CuO consisted of a myriad of nanotubes of 150-350 nm in diameter, over 2 μm in length and tens of nanometers in wall thickness. They were derived directly from the unique structural feature of $Cu(OH)_2$ in the form of nanotube forest. Fig. S1 clearly indicates that the surface morphology gradually evolved with reaction time. The
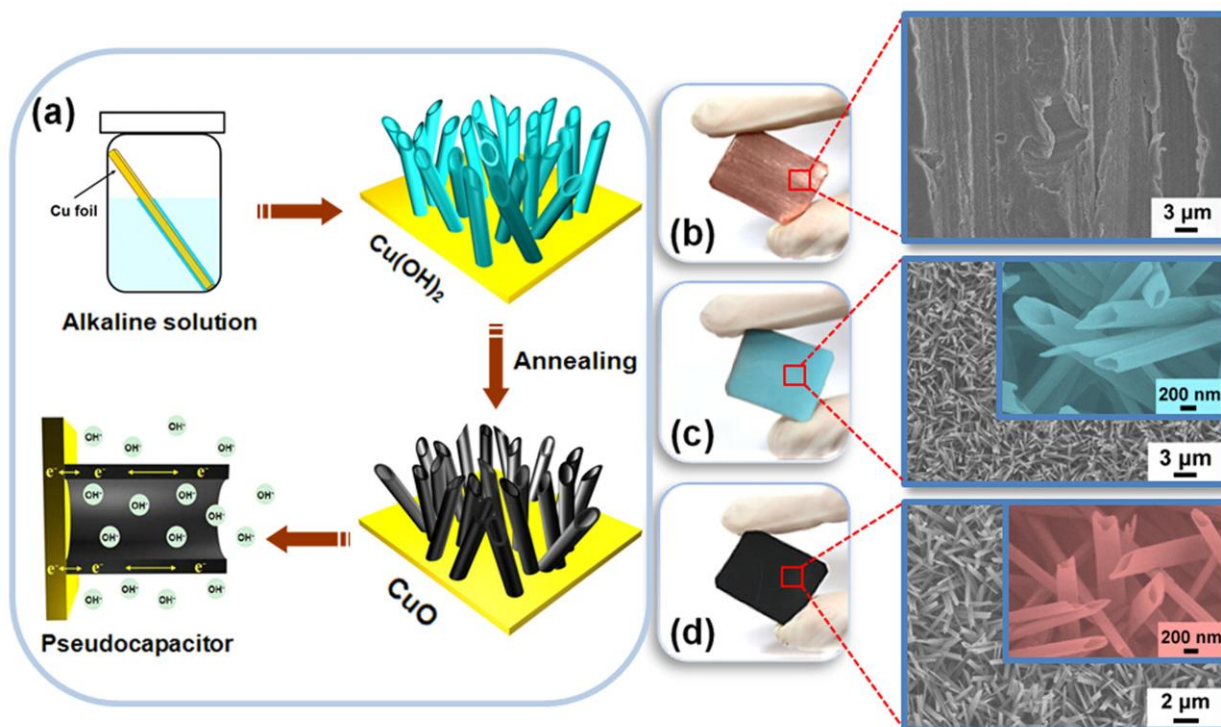
Fig. 1 (a) Schematic of the synthesis process of CuO nanotubes; (b-d) optical and SEM images of pristine copper foil, Cu(OH)$_2$ nanotubes on Cu foil, and CuO nanotubes on Cu foil.
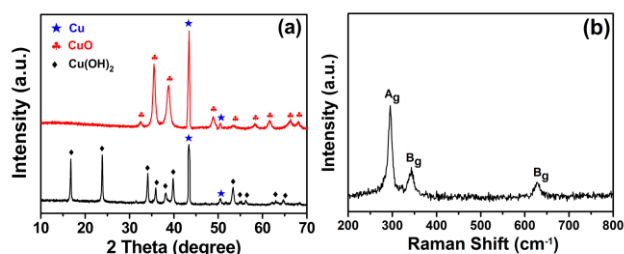
Fig. 2 (a) XRD patterns of as-prepared Cu(OH)$_2$ and CuO nanotubes directly grown on Cu foil; and (b) Raman spectrum of CuO nanotubes.

cleaned Cu foil exhibited a rough surface with some directionality (Figs. S1a, b). After 5 min of treatment, solid nanorods started
10 appearing sparsely on the surface (Figs. S1c, d). The nanorods became thicker and longer covering the surface in a directional manner with less blank surface after another 5 min of reaction (Fig. S1e). More interestingly, the solid rod tips started opening up at this stage (Fig. S1f). Finally, these nanorods were
15 transformed entirely into nanotubes with irregularly-shaped ends after 20 min of reaction, which densely covered the Cu foil surface (Figs. S1g, h). These numerous nanotubes were grown in the form of a forest with ample space in between, such that the electrolyte could have full access to and direct contacts with the
20 nanotubes for electrochemical reactions.

The TEM image of a single CuO nanotube shows a porous structure with a uniform wall thickness (Fig. S2a). The lattice fringe spacings of 0.233 and 0.26 nm marked in Fig. S2b correspond to the (111) and (002) planes of monoclinic CuO,
25 respectively. However, the lattice fringes were not continuous,

which is consistent with the porous nature of the nanotube. The selected area electron diffraction (SAED) pattern (inset of Fig. S2b) indicates that the porous nanotubes had a relatively ordered internal structure with the same orientation.[33, 34]

30 Fig. 2a shows the powder XRD patterns of Cu(OH)$_2$ and CuO nanotubes in the wide angle region. Both materials showed two strong peaks at 43.3^o and 50.4^o, arising from the Cu foil (JCPDS file No. 65-9026). All the other diffraction peaks for Cu(OH)$_2$ nanotubes are indexed to orthorhombic Cu(OH)$_2$ (JCPDS file No.
35 35-0505). After heat treatment, the peaks located at 32.5^o, 35.5^o, 38.7^o, 38.9^o, and 48.7^o are assigned to the (110), (002), (111), (200), and (202) planes of CuO phase (JCPDS file No. 45-0937), respectively. There were no other sharp peaks due to impurities, confirming high purity CuO nanotubes obtained in this study
40 using the mild *in situ* reaction strategy. The high purity nanotubes were further evidenced by the Raman result, as seen in Fig. 2b. The broad peak with a relatively high intensity at 295 cm^{-1} is assigned to A$_g$ band, while the two peaks at 342.8 and 628.5 cm^{-1} are assigned to 2B$_g$. The significant intensities of these peaks
45 indicate a single phase and high crystallinity of CuO nanotubes, in good agreement with the previous reports.[35, 36]

The results from the thermogravimetric and differential thermal analysis (TG-DTA) of Cu(OH)$_2$ nanotubes are shown in Fig. S3. The gradual weight loss of 1.4 % between 26 and 150 ^{o}C
50 resulted from the removal of physically adsorbed and chemically bound water. The rapid weight loss of 12.4% between 150 and 180 ^{o}C is ascribed to the decomposition of Cu(OH)$_2$ to become CuO nanotubes. The DTA curve showed a strong heat absorption peak at ~170 ^{o}C, consistent with the decomposition of Cu(OH)$_2$
55 nanotubes.[37] A further increase in temperature beyond 190 ^{o}C did
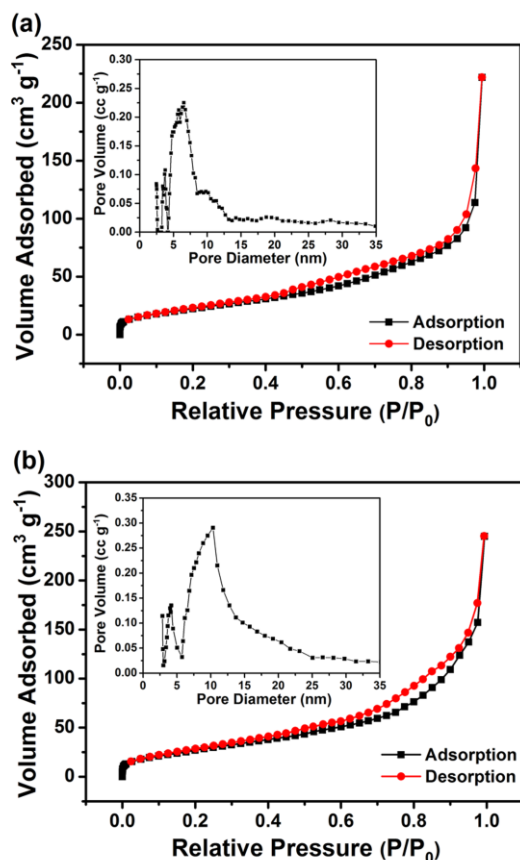
Fig. 3 Nitrogen adsorption/desorption isotherms of (a) Cu(OH)$_2$ nanotubes and (b) CuO nanotubes: the insets show the corresponding BJH pore size distributions.

[5] not present any weight loss, indicating complete decomposition below 190 ^{o}C which is considered an appropriate calcination temperature.

The N$_2$ adsorption/desorption isotherm curves were obtained to investigate the porous characteristics and textural properties. [10] According to the IUPAC classification of hysteresis loops,[38] Fig. 3 plots type IV isotherms with type H3 hysteresis loops. They do not exhibit any limited adsorption at relative pressures from 0 to 1, proving the presence of a typical hierarchical porosity.[39,40] An increase in slope at 0.6, especially for CuO nanotubes, [15] corresponds to capillary condensation, typical of mesoporous materials, while the further increase in adsorbed volume at higher relative pressures indicates inter-particle porosity. The BET surface area was much larger for CuO nanotubes (109.02 m^2 g^{-1}) than for Cu(OH)$_2$ nanotubes (41.84m^2 g^{-1}). The average pore [20] diameters of the two materials were positioned in the mesopore region: the maxima were centered between 3.76 and 6.54 nm for Cu(OH)$_2$ nanotubes, and between 4.15 and 10.34 nm for CuO nanotubes. Such well-developed pore structures are advantageous for energy storage and electrocatalysis applications since large [25] pore channels permit rapid electrolyte transport, while small pores offer more active sites for redox reactions.

The wettability test result shown in Fig. S4a presented a very low CA of 18.57^o on the surface of Cu(OH)$_2$. The CA with the CuO surface remained very low, 27.01^o (Fig. S4b). The low CAs [30] are attributed to the hydrophilic nature of both Cu(OH)$_2$ and CuO along with mesopores covering their surfaces,[41] confirming

excellent wettability of the nanotubes by aqueous electrolyte when they are employed as the electrode.[42]

Excellent energy storage performance

[35] The above ameliorating surface properties of the porous CuO nanotubes, including extremely large BET surface area, pore volume and excellent wettability, offered significant synergy on pseudocapacitive performance of the electrode, as shown in Fig. 4. The CV curves of the three different electrode materials obtained [40] at a scan rate of 10 mV s^{-1} (Fig. 4a) clearly indicate that the capacitive current of neat Cu foil was much lower than those of Cu(OH)$_2$ and CuO nanotube electrodes, confirming a negligible capacitance contribution of the Cu foil to the composite electrodes. The CuO nanotube electrode exhibited more distinct [45] redox peaks and a much larger enclosed area of the CV curve than those of the Cu(OH)$_2$ electrode. These findings imply that the former electrode would have a higher capacitance than the latter as the specific capacitance is proportional to the area of the CV curve.[43] The CV profiles given in Figs. 4b and 4c reveal that [50] the capacitance characteristics of both the nanotube electrodes are obviously different from that of the ideal rectangular shape for electric double-layer capacitance, suggesting their capacitances originating primarily from the Faradic redox reactions. The redox reactions involve in the transition between [55] Cu$^+$ and Cu^{2+} species associated with OH$^-$ions:[44]

$$Cu_2O + 2OH^- \longleftrightarrow 2CuO + H_2O + 2e^- \qquad (1)$$

With increasing scan rate, the current density increased while the shape of the CV curves remained largely unchanged except for the small shift of the peak position, presenting prominent [60] electrochemical reversibility and apparent high-rate performance. The specific capacitances (C_s) were calculated from the CV curves according to the equation:[45]

$$C_s = \frac{\int I dV}{v \Delta V m} \qquad (2)$$

[65] where I (A) is the response current, v (V s^{-1}) is the potential scan rate, ΔV (V) is the potential window, and m (g) is the mass of the active electrode material. It is noted that the specific capacitance of the CuO nanotube electrode gradually decreased from 564 to [70] 419 F g^{-1} when the scan rate was changed from 5 to 100 mV s^{-1} (Fig. 4d). The Cu(OH)$_2$ nanotube electrode presented an essentially similar trend with lower capacitances by 80-90 F g^{-1} than the corresponding values of the former electrode. The reduction in capacitance at high charge/discharge rates means that [75] all active species of the electrode did not involve in the redox process.

The galvanostatic charge/discharge curves obtained at a current density of 1 A g^{-1}(Fig. 4e) gave discharge times 5.04, 226.2 and 265.2 s for the Cu foil, Cu (OH)$_2$ and CuO nanotube electrodes, [80] respectively. This finding further demonstrates that Cu foil had a negligible capacitance while the CuO electrode exhibited better electrochemical performance than the Cu(OH)$_2$ electrode. Both the curves of the Cu(OH)$_2$and CuO electrodes were not ideal straight lines, suggesting the dominance of the pseudocapacitive [85] behavior. In addition, the sudden potential drop in the initial discharge period was caused by internal resistance of the electrodes.[46]Figs. 4f and g show the galvanostatic charge/discharge
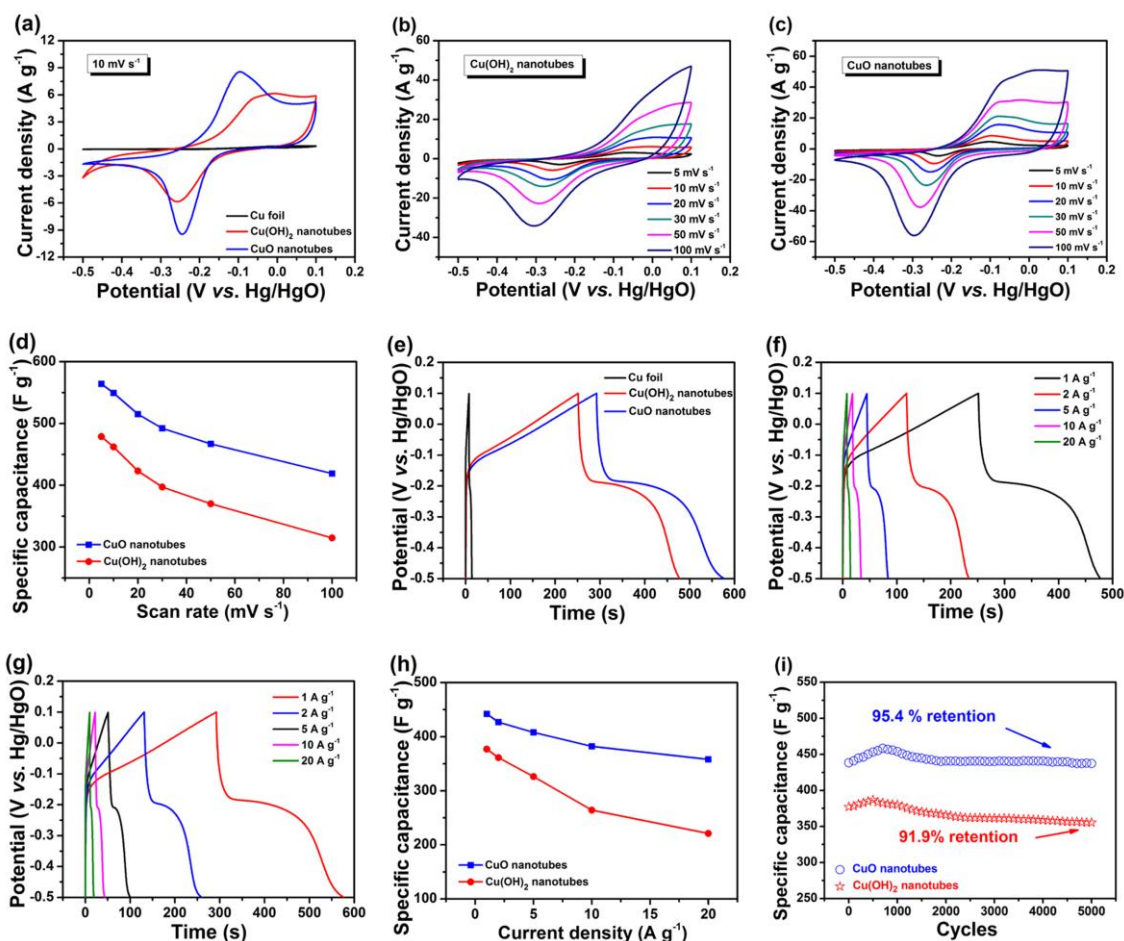
Fig.4 (a) CV curves of three electrode materials measured at 10 mVs⁻¹; CV curves of (b) Cu(OH)₂ and (c) CuO nanotube electrodes at different scan rates; (d) plots of specific capacitance of Cu(OH)₂ and CuO nanotube electrodes *vs* scan rate; (e) galvanostatic charge/discharge curves at 1 A g⁻¹; galvanostatic charge/discharge curves of (f) Cu(OH)₂ and (g) CuO nanotube electrodes at different current densities; (h) plots of specific capacitance of Cu(OH)₂ and CuO nanotube electrodes *vs* current density; and (i) cyclic performance of electrodes at 1 A g⁻¹.

curves of the Cu(OH)₂ and CuO electrodes at different current densities, respectively. The specific capacitances (C_s) were calculated at different applied current densities using the following equation:[3]

$$C_s = I\Delta t/\Delta Vm \qquad (3)$$

where I, Δt, ΔV and m refer to the constant discharge current, the total discharge time, the potential window and the mass of the electroactive materials, respectively. When the current density was changed from 1 to 20 A g⁻¹, the specific capacitance of the CuO nanotube electrode gradually decreased from 442 to 358 F g⁻¹ and likewise from 377 to 221 F g⁻¹ for the Cu(OH)₂ electrode, with remarkable capacity retention ratios of ~81% and ~59%, respectively (Fig. 4h). The higher the current density used, the more difference in capacitance between the two electrodes. This result further confirms that the porous CuO electrode with a larger surface area was more competent to boost electron transport when charged/discharged at faster rates. The common capacitance decrease resulting from the increase in current density is likely caused by the increase in potential drop due to the electrode resistance and the relatively less utilization of the active material at high current densities.[47]

The long-term cyclic stability of the electrodes was measured at a current density of 1 A g⁻¹ (Fig. 4i). Interestingly, the specific capacitance of both electrodes increased in the first several hundred cycles, which can be attributed to the gradual activation of the electrodes before reaching the full activation. The capacitance retention of the Cu(OH)₂ and CuO electrodes after 5000 cycles was 95.4% and 91.9% of the maximum value, respectively. The pseudocapacitive behavior is associated primarily with redox reactions of the cations in electrode materials.[48] Thus, the charge storage mechanisms of both the electrodes in SCs should be similar.

Judging from the fact that both electrodes have the same Cu²⁺ and similar nanotube structures, they should show similar electrochemical performance. Because the Cu(OH)₂ electrode possessed a relatively smaller surface area and lower porosity than the CuO counterpart, the kinetics of the ions would be slower with an inevitably lower capacitance. The difference in electrochemical performance of these two electrodes can also be understood from the Nyquist plot (Fig. 5a). The two impedance spectra were similar, being composed of one semicircle component
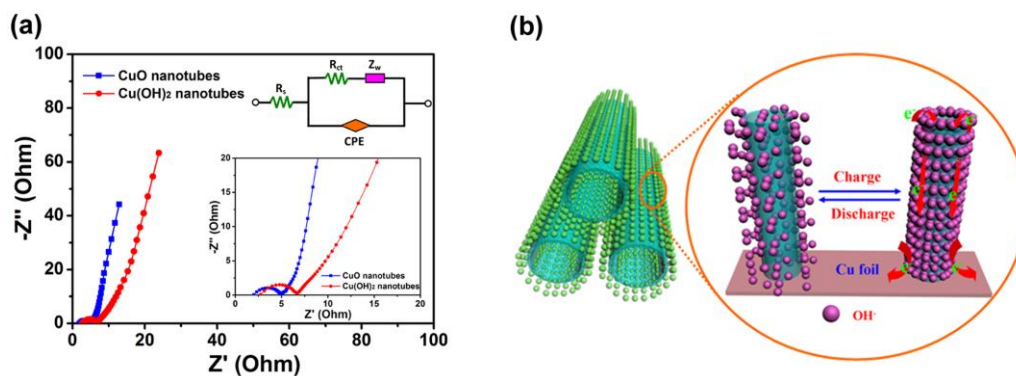
Fig. 5 (a) Electrochemical impedance spectra (EIS) of electrodes at open circuit potential; and (b) schematic of charge storage advantages of porous CuO nanotube electrodes.

each at high frequencies and a linear component each at low frequencies, further demonstrating the long-term electrochemical stability of these electrode materials.[49] The internal resistance (R_s) is the sum of the ionic resistance of electrolyte, the intrinsic resistance of active materials and the contact resistance at the active material/current collector interface,[50] and can be obtained from the intercept of the plots on the real axis. The semicircle of the Nyquist plot corresponds to the Faradic reactions and its diameter represents the interfacial charge transfer resistance (R_{ct}). The inset of Fig. 5a gives an equivalent circuit used to fit the EIS curves to measure R_s and R_{ct}, where Z_w and CPE are the Warburg impendence and the constant phase element, respectively.[51] The results are shown in Table S1, confirming much lower R_s and R_{ct} values for the CuO electrode than the Cu(OH)$_2$ electrode. Furthermore, the CuO electrode presented a higher slope and a shorter line in the low frequency region, suggesting faster OH$^-$ diffusion rates and smaller variation of diffusion paths. All these observations are directly related to the better overall electrochemical properties of the CuO electrode than the Cu(OH)$_2$ counterpart as discussed above with reference to Fig. 4.

Summarizing, the mechanism of charge transfer in the CuO nanotube electrode is schematically shown in Fig. 5b. The CuO nanotubes offer reliable one-dimensional pathways for charge carrier transport. The open-end nanotube structure combined with a large surface area and ample empty space in-between allows the relief of strains induced during the charge/discharge process and provides extremely large reaction sites between the active materials and the electrolyte.

To further demonstrate the long-term stability of the CuO nanotube electrode, the changes in morphology and impedance after 5000 cycles at 1.0 A g^{-1} were evaluated and the results are shown in Figs. S5 and S6. It is clearly seen that the nanotube forest was largely intact and attached firmly onto the Cu foil current collector after the repeated phase conversion reactions (Fig. S5). There was virtually no change in the detailed nanotube structure. When the Nyquist plots obtained after 1 and 5000 cycles are compared (Fig. S6), the R_s of the CuO electrode showed only a negligible increase from 1.71 to 1.83 Ω, manifesting an excellent conductivity of the electrolyte and a very low internal resistance of the composite electrode (Table S2). The R_{ct}, however, increased slightly more after 5000 cycles, probably as a result of the gradual formation of solid electrolyte interface films. Nevertheless, the CuO nanotube electrode remained remarkable cyclic stability, as seen from Fig. 4i.

Sensitive biosensory capability

The electrochemical performance of the CuO nanotube electrode as a non-enzymatic glucose biosensor was also investigated. Fig. 6a shows the linear-sweep voltammogram of the electrode in 0.1M KOH solution measured at a scan rate of 0.05 Vs^{-1}. Broad catalytic current peaks with a peak potential of about +0.5 V were observed, which might correspond to the Cu^{2+}/Cu^{3+} redox couple. The amperometric response linearly increased with increasing glucose concentration at all applied potentials. Furthermore, glucose oxidation occurred in the potential range of 0.4-0.8 V, where the oxidation wave for Cu^{2+}/Cu^{3+} was demonstrated.[31] All these observations prove that the CuO electrode was electrocatalytically active for glucose oxidation. Fig. 6b shows a typical amperometric response curve of the electrode when the glucose concentration was successively increased in a stepwise manner. The electrode exhibited a stable and immediate amperometric response to the changes in glucose concentration. As expected, the signal noise increased with increasing glucose concentration due to the accumulation of adsorbed intermediate species on the electrode surfaces.[52] The corresponding calibration curve is plotted in Fig. 6c, where a linear region was found between the concentrations 100μM and 3 mM with an equation: I (mA) = 0.1267 + 2.231C (mM) and a correlation coefficient of 0.999. The electrode presented an excellent sensitivity of 2231μAmM^{-1} cm^{-2} and a low detection limit of 1.07 μM (with a signal/noise ratio = 3). It should be noted that the detection limit is at least three orders of magnitude lower than the normal blood glucose level of 4.4-6.6 mM,[53] indicating that the CuO nanotube electrode is perfectly suited to electrochemical detection of blood glucose. Note that the sensitivity of our present sensing system is higher than that of other CuO materials,[54-57] as shown in Table S3. To test the stability and reproducibility of the sensor, we performed 20 successive measurements at a glucose concentration of 0.1 mM. It was found that the relative standard deviation (R. S. D.) was 2.3 %, indicating an acceptable reproducibility.

Another important analytical factor of a glucose sensor is the ability to discriminate the interference species from the real sample, such as ascorbic acid (AA), urea, lactose, uric acid (UA), and sodium chloride (NaCl), all of which usually coexist with glucose
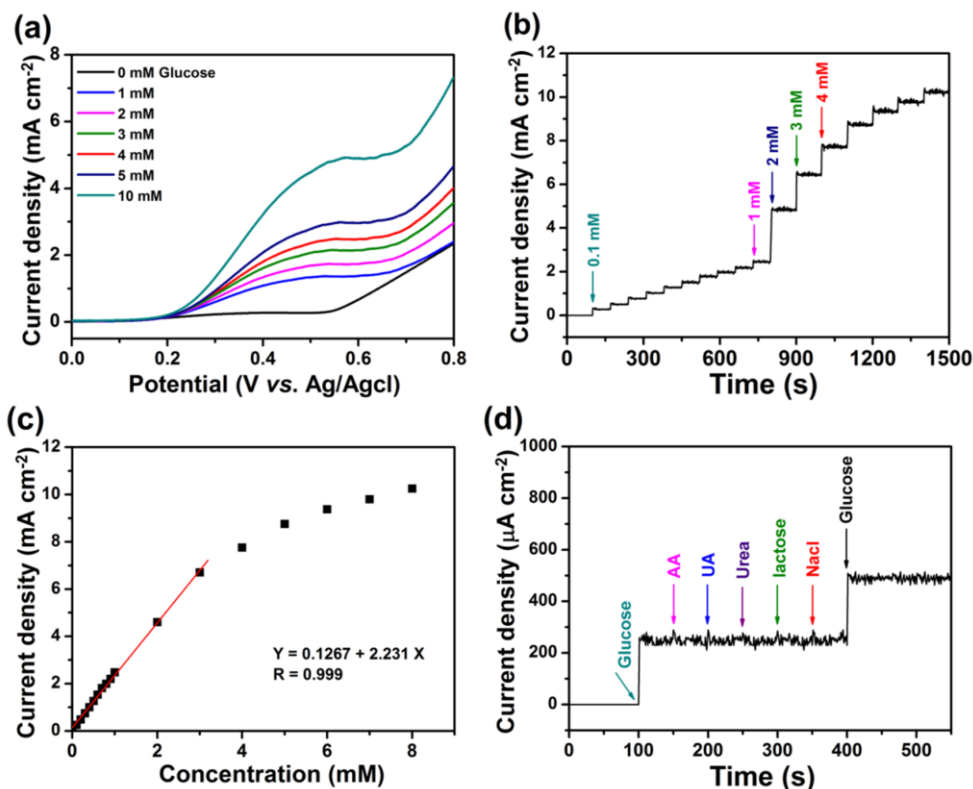
Fig. 6 (a) Linear-sweep voltammograms collected for CuO nanotube electrode at different glucose concentrations; (b) amperometric response of CuO nanotube electrode to the changes in glucose concentration in 0.1 M KOH at 0.50 V *vs.*Ag/AgCl; (c) current-glucose concentration calibration curve; and

5   (d) anti-interference property of CuO nanotube electrode upon stepwise addition of 10 μM AA, UA, urea, lactose and NaCl, followed by addition of 100 μM glucose solution.

in human blood. In view of the fact that the concentration of glucose in human blood is more than 30 times the interfering species,[58] the interference experiment was carried out by

10 successive addition of 0.1 mM of glucose and 0.01 mM of interfering species in the 0.1 M KOH solution. As shown in Fig. 6d, a distinct glucose response was observed while the responses to the interfering species were negligible compared to glucose addition. This observation confirms a satisfactory anti-interference

15 ability of the CuO nanotube-based glucose sensor.

Conclusions

We present a facile strategy for *in-situ* synthesis of low-cost, free-standing, binder-free CuO nanotube electrodes on a highly conductive Cu foil. The electrode material offered many

20 advantages, including highly porous structure, large surface area, abundant empty space, short and fast electron transport paths and total elimination of both inactive materials and extra processing steps. These advantages make them ideal electrodes for SCs and NGBs. The electrode exhibited excellent electrochemical

25 properties, including a remarkable specific capacitance of 382 F g^{-1} at a current density of 10 A g^{-1} and a response to glucose at a linear range of 100 μM to 3 mM with an outstanding sensitivity of 2231 μA mM^{-1} cm^{-2}. The above findings may open up a new avenue for practical application of CuO nanotube electrodes in

30 the next-generation SCs and NGBs.

Notes and references

[a]*School of Physics and Electronic Engineering, Xinyang Normal University, Xinyang 464000, P. R. China. E-mail:ysluo@xynu.edu.cn*

40 [b]*Key Laboratory of Advanced Micro/Nano Functional Materials, Xinyang Normal University, Xinyang 464000, P. R. China.*
[c]*School of Material Science and Engineering, Hebei University of Technology, Tianjin 300130, P.R.China. E-mail:tangcc@hebut.edu.cn*
[d]*School of Materials Science and Technology, China University of*

45 *Geosciences, Beijing 100083, P. R. China.*
[e]*College of Chemistry and Chemical Engineering, Luoyang Normal University, Luoyang 471022, P. R. China.*
[f]*Department of Mechanical and Aerospace Engineering, The Hong Kong University of Science and Technology, Clear Water Bay, Kowloon, Hong*

50 *Kong, P. R. China.*

† Electronic Supplementary Information (ESI) available: TG-DTA curves, hydrophilicity test, FESEM images of the growth process of Cu(OH)2 nanotubes, FESEM images and electrochemical impedance spectra of

55 CuO nanotube electrodes.

1 S. Yuan, X. L. Huang, D. L. Ma, H. G. Wang, F. Z. Meng and X. B. Zhang, *Adv. Mater.*, 2014, **26**, 2273.

2 Z. Li, Z. W. Xu, H. L. Wang, J. Ding, B. Zahiri, C. M. B. Holt, X. H. Tan and D. Mitlin, *Energy Environ. Sci.*, 2014, **7**, 1708.

3 M. J. Deng, P. J. Ho, C. Z. Song, S. A. Chen, J. F. Lee, J. M. Chen and K. T. Lu, *Energy Environ. Sci.*, 2013, **6**, 2178.

4 X. Y. Xie, C. Zhang, M. B. Wu, Y. Tao, W. Lv and Q. H. Yang, *Chem. Commun.*, 2013, **49**, 11092.

5 H. L. Wang, Q. M. Gao and L. Jiang, *Small*, 2011, **7**, 2454.

6 P. Simon and Y. Gogotsi, *Nat. Mater.*, 2008, **7**, 845.

7 X. H. Lu, D. Z. Zheng, T. Zhai, Z. Q. Liu, Y. Y. Huang, S. L. Xie and Y. X. Tong, *Energy Environ. Sci.*, 2011, **4**, 2915.

8 W. Chen, R. B. Rakhi, L. B. Hu, X. Xie, Y. Cui and H. N. Alshareef, *Nano Lett.*, 2011, **11**, 5165.

9 Y. M. Chen, X. Y. Li, X. Y. Zhou, H. M. Yao, H. T. Huang, Y. W. Mai, and L. M. Zhou, *Energy Environ. Sci.*, 2014, **DOI:** 10.1039/C4EE00148F.

10 L. Wang, H. M. Ji, S. S. Wang, L. J. Kong, X. F. Jiang and G. Yang, *Nanoscale*, 2013, **5**, 3793.

11 Q. F. Wang, X. F. Wang, B. Liu, G. Yu, X. J. Hou, D. Chen and G. Z. Shen, *J. Mater. Chem. A*, 2013, **1**, 2468.

12 Y. J. Chen, B. H. Qu, L. L. Hu, Z. Xu, Q. H. Li and T. H. Wang, *Nanoscale*, 2013, **5**, 9812.

13 Y. S. Luo, D. Z. Kong, Y. L. Jia, J. S. Luo, Y. Lu, D. Y. Zhang, K. W. Qiu, C. M. Li and T. Yu, *RSC Adv.*, 2013, **3**, 5851.

14 H. B. Wu, H. Pang and X. W. Lou, *Energy Environ. Sci.*, 2013, **6**, 3619.

15 X. J. Zhang, W. H. Shi, J. X. Zhu, D. J. Kharistal, W. Y. Zhao, B. S. Lalia, H. H. Hng and Q. Y. Yan, *ACS Nano*, 2011, **5**, 2013.

16 G. L. Wang, J. C. Huang, S. L. Chen, Y. Y. Gao and D. X. Cao, *J. Power Sources*, 2011, **196**, 5756.

17 D. P. Dubal, G. S. Gund, R. Holze, H. S. Jadhav, C. D. Lokhande and C. J. Park, *Dalton Trans.*, 2013, **42**, 6459.

18 D. Pradhan, F. Niroui and K. T. Leung, *ACS Appl. Mater. Int.*, 2010, **2**, 2409.

19 M. Lee, S. Kabilan, A. Hussain, X. P. Yang, J. Blyth and C. Lowe, *Anal. Chem.*, 2004, **76**, 5748.

20 C. S. Rout, A. Govindaraj and C. N. R. Rao, *J. Mater. Chem.*, 2006, **16**, 3936.

21 L. Q. Luo, L. M. Zhu and Z. X. Wang, *Bioelectrochemistry*, 2012, **88**, 156.

22 J. C. Pickup, F. Hussain, N. D. Evans and N. Sachedina, *Biosens. Bioelectron.*, 2005, **20**, 1897.

23 X. J. Zhang, A. X. Gu, G. F. Wang, Y. Wei, W. Wang, H. Q. Wu and B. Fang, *CrystEngComm*, 2010, **12**, 1120.

24 Y. X. Li, X. H. Niu, J. Tang, M. B. Lan and H. L. Zhao, *Electrochim. Acta*, 2014, **130**, 1.

25 Y. Xia, W. Huang, J. F. Zheng, Z. J. Niu, Z. L. Li, *Biosens. Bioelectron.*, 2011, **26**, 3555.

26 J. Wang, *Chem. Rev.*, 2008, **108**, 814.

27 P. Si, X. C. Dong, P. Chen and D. H. Kim, *J. Mater. Chem. B*, 2013, **1**, 110.

28 W. Z. Jia, M. Guo, Z. Zheng, T. Yu, Y. Wang and E.G. Rodriguez, *Electranalysis*, 2008, **20**, 2153.

29 C. Batchelor-McAuley, Y. Du, G. G. Wildgoose and R. G. Compton, *Sens. Actuators B:Chem.*, 2008, **135**, 230.

30 L. Zhang, Y. H. Ni and H. Li, *Microchim. Acta*, 2010, **171**, 103.

31 Z. J. Zhuang, X. D. Su, H. Y. Yuan, Q. Sun, D. Xiao and M. M. F. Choi, *Analyst*, 2008, **133**, 126.

32 Y. J. Yang, W. K. Li and X. H. Chen, *J. solid state electrochem.*, 2012, **16**, 2877.

33 Y. M. Sun, X. L. Hu, W. Luo and Y. H. Huang, *J. Mater. Chem.*, 2012, **22**, 13826.

34 Y. M. Zhang, W. X. Zhang, M. Li, Z. H. Yang, G. D. Chen and Q. Wang, *J. Mater. Chem. A*, 2013, **1**, 14368.

35 M. A. Dar, Q. Ahsanulhaq, Y. S. Kim, J. M. Sohn, W. B. Kim and H. S. Shin, *Appl. Surf. Sci.*, 2009, **255**, 6279.

36 X. Wang, G. Xi, S. Xiong, Y. Liu, B. Xi, W. Yu, Y. Qian, *Cryst. Growth Des.*, 2007, **7**, 930.

37 Y. X. Zhang, M. Huang, F. Li and Z. Q. Wen, *Int. J. Electrochem. Sci.*, 2013, **8**, 8645.

38 W. Xiong, M. X. Liu, L. H. Gan, Y. K. Lv, Y. Li, L. Yang, Z. J. Xu, Z. X. Hao, H. L. Liu and L. W. Chen, *J. Power Sources*, 2011, **196**, 10461.

39 D. Grosso, G. Illia, E. L. Crepaldi, B. Charleux and C. Sanchez, *Adv. Funct. Mater.*, 2003, **13**, 37.

40 J. R. Matos, M. Kruk, L. P. Mercuri, M. Jaroniec, L. Zhao, T. Kamiyama, O. Terasaki, T. J. Pinnavaia and Y. Liu, *J. Am. Chem. Soc.*, 2003, **125**, 821.

41 L. Feng, S. H. Li, Y. S. Li, H. J. Li, L. J. Zhang, J.Zhai, Y. L. Song, B. Q. Liu, L. Jiang and D. B. Zhu, *Adv. Mater.*, 2002, **14**, 1857.

42 P. M. Kulal, D. P. Dubal, C. D. Lokhande and V. J. Fulari, *J. Alloys Compd.*, 2011, **509**, 2567.

43 J. W. Lee, A. S. Hall, J. D. Kim and T. E. Mallouk, *Chem. Mater.*, 2012, **24**, 1158.

44 G. L. Wang, J. C. Huang, S. L. Chen, Y. Y. Gao and D. X. Cao, *J. Power Sources*, 2011, **196**, 5756.

45 H. B. Wu, H. Pang and X. W. Lou, *Energy Environ. Sci.*, 2013, **6**, 3619.

46 Y. H. Li, S. Chang, X. L. Liu, J. C. Huang, J. L. Yin, G. L. Wang and D. X. Cao, *Electrochim. Acta*, 2012, **85**, 393.

47 J. Huang, J. Zhu, K. Chen, Y. Xu, D. Cao and G. Wang, *Electrochim. Acta*, 2012,**75**, 273.

48 M. Song, S. Cheng, H. Chen, W. Qin, K. Nam, S. Xu, X. Yang, A. Bongiorno, J. Lee, J. Bai, *Nano Lett.*, 2012, **12**, 3483.

49 Y. S. Luo, J. S. Luo, J, Jiang, W. W. Zhou, H. P. Yang, X. Y. Qi, H. Zhang, H. J. Fan, D. Y. W. Yu, C. M. Li and T. Yu, *Energy Environ. Sci.*, 2012, **5**, 6559.

50 A. Lahe ä är, A. J änes and E. Lust, *Electrochim. Acta*, 2012, **82**, 309.

51 B. Zhang, Y. Liu, Z. D. Huang, S. W. Oh, Y. Yu, Y. W. Mai and J. K. Kim, *J. Mater. Chem.*, 2012, **22**, 12133.

52 L. C. Jiang, W. D. Zhang, *Biosens. Bioelectron.*, 2010, **25**, 1402.

53 K. M. E. Khatiba and R. M. A. Hameed, *Biosens. Bioelectron.*, 2011, **26**, 3542.

54 J. Yang, L. C. Jiang, W. D. Zhang, S. Gunasekarana, *Talanta*, 2010, **82**, 25.

55 W. Wang, L. L. Zhang, S. F. Tong, X. Li, W. B. Song, *Biosens. Bioelectron.*, 2009, **25**, 708.

56 E. Reitz, W. Z. Jia, M. Gentile, Y. Wang, Y. Lei, *Electroanalysis*, 2008, **20**, 2482.

57 S. Liu, J. Q. Tian, L. Wang, X. Y. Qin, Y. W. Zhang, Y. L. Luo, A. M.Asiri, A. O. Al-Youbi, X. P. Sun, *Catal. Sci. Technol.*, 2012, **2**, 813.

58 L. Qian, J. F. Mao, X. Q. Tian, H. Y. Yuan and D. Xiao, *Sens. Actuators B*, 2013, **176**, 952.